

VLBI Diagnostics of Off-axis Jets in Radio Flares of Tidal Disruption Events

TATSUYA MATSUMOTO¹

¹*Department of Astronomy, School of Science, The University of Tokyo, Bunkyo-ku, Tokyo 113-0033, Japan*

ABSTRACT

The origin of late-time radio flares in tidal disruption events remains unclear. In particular, the peculiar radio flare observed in AT2018hyz has motivated two leading scenarios: a delayed outflow launched ~ 1000 days after discovery, or an off-axis relativistic jet directed far from our line of sight. Very long baseline interferometry (VLBI) imaging provides the most direct way to distinguish between these scenarios. In this paper, we calculate synthetic radio images for both models and examine their observational signatures. The motion of the emission centroid is the most powerful diagnostic for breaking the degeneracy. In the delayed-outflow scenario, the centroid motion is confined within a non-relativistic distance, whereas in the off-axis jet scenario it exhibits apparent superluminal motion. Detecting such superluminal motion would therefore provide a smoking-gun signature of the off-axis jet interpretation. We also find that the jet image exhibits characteristic features, including a non-monotonic evolution of the image aspect ratio. These results are expected to be generic and applicable to other jetted explosions, such as microquasars and gamma-ray bursts.

Keywords: XXX

1. INTRODUCTION

Recent observations have revealed that a significant fraction of optical tidal disruption events (TDEs; M. J. Rees 1988) are accompanied by radio flares appearing as late as ~ 1000 days after discovery (Y. Cendes et al. 2024; see also A. Horesh et al. 2021a,b; Y. Cendes et al. 2022; A. J. Goodwin et al. 2023; C. T. Christy et al. 2024; F. Zhang et al. 2024; W. W. Golay et al. 2025; A. Hajela et al. 2025; A. J. Goodwin et al. 2025). Several ideas have been proposed for the origin of these late-time radio flares, including delayed outflows produced by delayed disk formation or state transitions in the disk (Y. Cendes et al. 2022; K. D. Alexander et al. 2025; S. C. Wu et al. 2025), prompt outflows interacting with a circum-nuclear medium (CNM) with a non-monotonic density profile (T. Matsumoto & T. Piran 2024; J. Zhuang et al. 2025), and off-axis relativistic jets (T. Matsumoto & T. Piran 2023; I. Sfaradi et al. 2024). Despite these efforts, their physical origin remains uncertain.

Among the late-time radio flares, AT2018hyz stands out as a particularly remarkable event (Y. Cendes et al. 2022; I. Sfaradi et al. 2024; Y. Cendes et al. 2025). After ~ 1000 days of non-detection, a radio flare suddenly emerged with a sharply rising light curve and an unusually high luminosity, comparable to that of jetted TDEs (T. Eftekhari et al. 2018; Y. Cendes et al. 2021). As one of the earliest identified examples of late-time flares,

this event was initially interpreted as being powered by a delayed outflow (Y. Cendes et al. 2022). T. Matsumoto & T. Piran (2023) further demonstrated that an off-axis relativistic jet (e.g., D. Giannios & B. D. Metzger 2011) can also reproduce the observed properties. At present, both scenarios remain viable and cannot be distinguished using the radio light curve and spectrum alone (Y. Cendes et al. 2025).

T. Matsumoto & T. Piran (2023) proposed that radio imaging with very long baseline interferometry (VLBI) could provide a direct diagnostic of the origin of the radio emission in AT2018hyz. VLBI observations have played a crucial role in revealing the nature of relativistic transients, including Galactic microquasars (I. F. Mirabel & L. F. Rodríguez 1994; S. J. Tingay et al. 1995; see also R. Fender 2006) and binary neutron star (BNS) mergers (K. P. Mooley et al. 2018; G. Ghirlanda et al. 2019). In particular, the BNS merger GW170817 has heightened interest in radio imaging and motivated numerous theoretical studies, using both (semi-)analytical (R. Gill & J. Granot 2018; J. J. Fernández et al. 2022; T. Govoren-Segal & E. Nakar 2023; G. Sadeh et al. 2024) and numerical approaches (J. Zrake et al. 2018; J. Granot et al. 2018; J. J. Fernández et al. 2022; V. Nedora et al. 2023). The same techniques are applicable to TDEs.

In this paper, we compute radio images of late-time radio flares in TDEs using a semi-analytical framework. In the context of TDEs, several previous studies have calculated synthetic images based on simulations (e.g.,

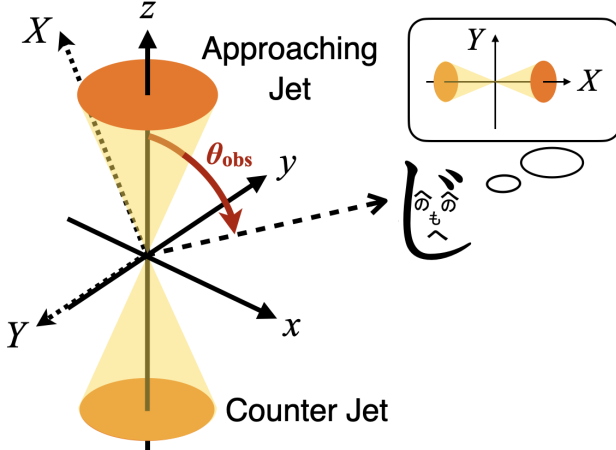


Figure 1. A schematic picture of the adopted coordinate system in our calculation. For a jet geometry, the jet is assumed to have a bipolar structure and each jet propagates along z axis. An observer is located within the xz plane, whose viewing angle θ_{obs} is measured from the z axis. The incoming (traveling into the positive z direction) and outgoing jets are called an approaching and counter jets, respectively. The coordinate system of the sky (XY) plane is defined so that the approaching jet always propagates into the positive X direction.

P. Mimica et al. 2015; F. F. Hu et al. 2025; G. Mou & X. Shu 2025), but did not carry out a detailed analysis of their properties. Moreover, recent VLBI observations of TDE radio flares (W. W. Golay et al. 2025; A. Hajela et al. 2025) further motivate a detailed theoretical investigation of their expected imaging signatures. Our approach allows us to isolate key physical effects and clarify the observational diagnostics that can distinguish between different scenarios.

The structure of the paper is as follows. In Section 2, we describe the method used to calculate the radio images as well as light curve and spectrum. In Section 3, we present radio images of AT2018hyz based on two different models. We discuss the very late-time evolution of the radio images and their implications in Section 4, and summarize our findings in Section 5.

2. METHOD

Light curves and images of synchrotron-emitting outflows have been calculated by many authors at various levels of approximation. In this study, we assume that the outflow is piecewise spherical; that is, each fluid element evolves as though it were part of a spherically symmetric outflow. We further assume that the emitting region is a thin shell, and do not consider any angular structure (but see e.g., A. Tchekhovskoy et al. 2014; O. Teboul & B. D. Metzger 2023; W. Lu et al. 2024).

2.1. Dynamics

The dynamics of the outflow is calculated under the piecewise spherical approximation. This is justified when the outflow is highly relativistic. However, for a jetted outflow, when its Lorentz factor becomes smaller than the inverse of the half opening angle, the jet starts to expand laterally (e.g., J. E. Rhoads 1999; J. Granot & T. Piran 2012). We neglect this sideway expansion in this paper, and assume that the jet propagates keeping its original shape. For TDE jets, this might be allowed because some jetted TDEs do not show signatures of the lateral expansion (E. Berger et al. 2012; T. Matsumoto & B. D. Metzger 2023).

We calculate the outflow's dynamics based on the energy conservation (T. Piran et al. 2013), which is adopted in our previous studies (R. Ricci et al. 2021; G. Bruni et al. 2021; A. Y. Q. Ho et al. 2025). For a top-hat jet, which has uniform energy and Lorentz factor distribution over its solid angle, the dynamics is characterized by the initial kinetic energy E_{ej} and Lorentz factor Γ_0 , and the CNM density profile $n(r)$. Note here E_{ej} is the isotropic-equivalent energy, defined as the energy the outflow would have if it covered a solid angle of 4π . Given the initial energy and Lorentz factor, the (isotropic-equivalent) mass of the outflow is given by the relation:

$$E_{\text{ej}} = (\Gamma_0 - 1)M_{\text{ej}}c^2 , \quad (1)$$

where c is the speed of light. The outflow expands sweeping up the CNM and unless the radiative energy loss is significant, its total energy at a radius R is given by

$$E_{\text{ej}} = (\Gamma - 1)[M_{\text{ej}} + \Gamma M(R)]c^2 , \quad (2)$$

where the swept-up CNM mass is

$$M(R) = \int^R 4\pi r^2 m_p n(r) dr . \quad (3)$$

Here m_p is the proton mass. Eq. (2) gives the outflow velocity, which is used to obtain the radius:

$$R(t) = \int^t \beta(t)c dt , \quad (4)$$

where t is the lab-frame time.

2.2. Flux

Once the dynamics is determined, the observed flux is calculated by integrating the emissivity over the emitting volume. The following method is largely based on H. van Eerten et al. (2010); K. Takahashi et al. (2022) but we account for the cosmological effect explicitly.

The flux is formally given by the integration of the intensity over the solid angle subtended by an emitting

source (G. B. Rybicki & A. P. Lightman 1979):

$$F_{\nu_{\text{obs}}} = \int I_{\nu_{\text{obs}}} d\hat{\Omega} , \quad (5)$$

where I_ν is the intensity and ν_{obs} is the observed frequency. The intensity is given by the radiative transfer equation:

$$\frac{dI_\nu}{ds} = -\alpha_\nu I_\nu + j_\nu , \quad (6)$$

where ν is the lab-frame frequency and related to ν_{obs} by $\nu_{\text{obs}} = \nu/(1+z)$. Under the thin-shell approximation, the absorption coefficient α_ν and emissivity j_ν may be assumed to be constant, and one can obtain

$$I_\nu = \frac{j_\nu}{\alpha_\nu} (1 - e^{-\tau_\nu}) \text{ and } \tau_\nu = \int \alpha_\nu ds = \alpha_\nu \Delta s , \quad (7)$$

where τ_ν and Δs are the optical depth and the shell width along the direction to the observer, respectively. From the Lorentz invariance of I_ν/ν^3 , the observed intensity is given by $I_{\nu_{\text{obs}}} = I_\nu/(1+z)^3$. Plugging above equations into Eq. (5), one obtains

$$F_{\nu_{\text{obs}}} = \frac{(1+z)}{d_L^2} \int j_\nu \left(\frac{1 - e^{-\tau_\nu}}{\tau_\nu} \right) dV . \quad (8)$$

where $dV = dS \Delta s$ is the volume element and dS is the emitting surface area projected on the sky plane. The latter is related to the solid angle by $d\hat{\Omega} = dS/d_A^2$. Here d_L and $d_A = d_L/(1+z)^2$ are the luminosity and angular diameter distances, respectively.

The absorption coefficient and emissivity are evaluated in the fluid rest frame. Quantities at the lab and fluid rest frames are related by the Lorentz transformation: $\nu = \delta_D \nu'$, $\alpha_\nu = \delta_D^{-1} \alpha'_{\nu'}$, and $j_\nu = \delta_D^2 j'_{\nu'}$, where the quantities in the fluid rest frame are denoted with a prime, and the relativistic Doppler factor is defined by

$$\delta_D \equiv \frac{1}{\Gamma(1-\beta\mu)} . \quad (9)$$

Here Γ and β are the Lorentz factor and normalized velocity of the fluid element, respectively, and μ is the cosine of the angle between the direction of the fluid motion and the observer's line of sight in the lab frame. The expressions of $\alpha'_{\nu'}$ and $j'_{\nu'}$ are given in Appendix A.

We introduce the spherical coordinate whose polar axis is aligned to the jet axis, and rewrite the volume element by $dV = R^2 \Delta R d\Omega$. Here ΔR is the shell width along the radial direction, which is given by the conservation of the particle number (H. van Eerten et al. 2010; K. Takahashi et al. 2022):

$$\Delta R = \frac{R}{4(3-k)\Gamma^2(1-\beta\mu)} . \quad (10)$$

Here we consider the case where the CNM has a power-law radial dependence, $n(r) \propto r^{-k}$. The shell widths along the different directions are related by $\Delta s = \Delta R/\mu$.

The integration of Eq. (8) should be carried out by taking into account the light traveling effect. A photon emitted at lab time t from a fluid element with μ is received by the observer at observer time of T when the following condition is satisfied:

$$\frac{T}{1+z} = t - \frac{\mu R(t)}{c} . \quad (11)$$

For given observer time T , the set of radii $R(t)$ obtained for different μ forms a surface, commonly referred to as the equal-arrival-time surface (EATS). Note that in the coordinate system in Fig. 1, μ is simply given by

$$\mu = \mathbf{n}_{\text{obs}} \cdot \mathbf{e}_r = \cos \varphi \sin \theta \sin \theta_{\text{obs}} + \cos \theta \cos \theta_{\text{obs}} ,$$

where

$$\begin{aligned} \mathbf{n}_{\text{obs}} &= (\sin \theta_{\text{obs}}, 0, \cos \theta_{\text{obs}}) , \\ \mathbf{e}_r &= (\cos \varphi \sin \theta, \sin \varphi \sin \theta, \cos \theta) . \end{aligned}$$

2.3. Image

To describe the image, we introduce a new (X, Y) coordinate as shown in Fig. 1. The X axis is defined so that it coincides with the axis of an approaching jet. The basis vectors of this coordinate are given by

$$\begin{aligned} \mathbf{e}_X &= (-\cos \theta_{\text{obs}}, 0, \sin \theta_{\text{obs}}) , \\ \mathbf{e}_Y &= (0, -1, 0) , \end{aligned}$$

and a fluid element at $\mathbf{R} = R \mathbf{e}_r$ is projected to

$$\begin{aligned} X &= \mathbf{R} \cdot \mathbf{e}_X = R(-\cos \varphi \sin \theta \cos \theta_{\text{obs}} + \cos \theta \sin \theta_{\text{obs}}) , \\ Y &= \mathbf{R} \cdot \mathbf{e}_Y = -R \sin \varphi \sin \theta . \end{aligned}$$

On the sky plane, a corresponding angular size is given by $\hat{X} = X/d_A$.

The flux is formally given by

$$F_{\nu_{\text{obs}}} = \int \frac{d^2 F_{\nu_{\text{obs}}}}{dXdY} dXdY = \int \frac{d^2 F_{\nu_{\text{obs}}}}{dXdY} \frac{\partial(X, Y)}{\partial(\theta, \varphi)} d\theta d\varphi . \quad (12)$$

Here the Jacobian is given by

$$\begin{aligned} \frac{\partial(X, Y)}{\partial(\theta, \varphi)} &= |\mathbf{N} \cdot \mathbf{n}_{\text{obs}}| \\ &= R \frac{\partial R}{\partial \theta} (\cos \theta_{\text{obs}} \sin^2 \theta - \sin \theta_{\text{obs}} \sin \theta \cos \theta \cos \varphi) \\ &\quad + R \frac{\partial R}{\partial \varphi} \sin \theta_{\text{obs}} \sin \varphi \\ &\quad + R^2 (\cos \theta_{\text{obs}} \sin \theta \cos \theta + \sin \theta_{\text{obs}} \sin^2 \theta \cos \varphi) , \end{aligned} \quad (13)$$

and \mathbf{N} is the normal vector to the EATS given by

$$\mathbf{N} = -R \sin \theta \frac{\partial R}{\partial \theta} \frac{\partial \mathbf{e}_r}{\partial \theta} - \frac{R}{\sin \theta} \frac{\partial R}{\partial \varphi} \frac{\partial \mathbf{e}_r}{\partial \varphi} + R^2 \sin \theta \mathbf{e}_r . \quad (14)$$

Note R denotes the radius of the EATS, $R_{\text{EATS}}(\theta, \varphi)$ given by Eq. (11). By comparing Eqs. (8) and (12), one can obtain the expression of the intensity:

$$I_{\nu_{\text{obs}}} = \frac{d^2 F_{\nu_{\text{obs}}}}{d \hat{X} d \hat{Y}} = \frac{\delta_{\text{D}}^2 j'_{\nu'}}{(1+z)^3} \left(\frac{1-e^{-\tau_{\nu}}}{\tau_{\nu}} \right) \frac{R^2 \Delta R \sin \theta}{|\mathbf{N} \cdot \mathbf{n}_{\text{obs}}|} . \quad (15)$$

Once an intensity distribution is obtained, the location of the emission centroid on the sky is calculated by

$$(\hat{X}_{\text{cen}}, \hat{Y}_{\text{cen}}) = \frac{\int (\hat{X}, \hat{Y}) I_{\nu_{\text{obs}}} d \hat{X} d \hat{Y}}{\int I_{\nu_{\text{obs}}} d \hat{X} d \hat{Y}} . \quad (16)$$

In particular, for an axisymmetric jet considered in this study, the emission centroid is always on the X -axis ($\hat{Y}_{\text{cen}} = 0$).

3. IMAGE OF TDE RADIO FLARE: APPLICATION TO AT2018HYZ

We calculate images of TDE radio flares by using the method in the previous section. Our main focus is on investigating the origin of late-time radio flares in TDEs, in particular, AT2018hyz showing one of the brightest radio flares (Y. Cendes et al. 2022; I. Sfaradi et al. 2024; Y. Cendes et al. 2025). AT2018hyz was discovered as an optical TDE, having a typical time evolution with a peak bolometric luminosity of $\simeq 10^{44} \text{ erg s}^{-1}$ (S. Gomez et al. 2020; P. Short et al. 2020; S. van Velzen et al. 2021; E. Hammerstein et al. 2023). A prompt radio followup at $\simeq 30$ days reported no detection, but a long-term monitoring revealed a sudden brightening ~ 1000 days after discovery (Y. Cendes et al. 2022; I. Sfaradi et al. 2024; Y. Cendes et al. 2025). The radio light curve shows a rapid rise $F_{\nu} \propto T^5$ and the spectra are fitted by a single-peak spectrum implying a synchrotron self-absorption (SSA) signature. The recent observation at $\simeq 2000$ days confirms that the light curve is still rising but at a little slower pace $\propto T^3$, and its luminosity is comparable to jetted TDEs (Y. Cendes et al. 2025).

Such an onset of the radio flare as late as ~ 1000 days was totally unexpected, and several scenarios have been proposed. One possibility is that the radio emitting outflow was launched after a delay of ~ 1000 days since the optical flare. This scenario is motivated by the result of the equipartition analysis (R. Barniol Duran et al. 2013; Y. Cendes et al. 2022). The inferred radial evolution suggests that the outflow was launched not at the time of optical discovery, but rather $\simeq 700$ days later with a Newtonian velocity (Y. Cendes et al. 2022, 2025). In this case, a state transition of an accretion disk may be

responsible for launching the outflow with the significant delay (K. D. Alexander et al. 2025). In other scenario, the radio outflow is a relativistic jet launched around the optical discovery but toward a different direction from our line of sight. Due to the off-axis effect, the radio flux is initially suppressed until it decelerates. This possibility is pointed out by T. Matsumoto & T. Piran (2023), who generalized the equipartition method to arbitrary viewing angles. Subsequent forward-modeling studies also confirmed this scenario (I. Sfaradi et al. 2024; Y. Sato et al. 2024; Y. Cendes et al. 2025). There are also other scenarios such as an interaction between a prompt-launched outflow and a gas cloud at some distance from the galactic center (e.g., J. Zhuang et al. 2025), but we focus on the scenarios of outflows interacting with CNM.

The current observations with radio light curve and spectra cannot discriminate the delayed outflow and off-axis jet scenarios, and they are still remain viable explanations (Y. Cendes et al. 2025). The most direct way to distinguish between them is through radio imaging with VLBI. Motivated by this, we compute radio images for both scenarios and quantitatively examine the differences between them.

3.1. Light Curve & Spectrum

We begin by fitting the light curve and spectrum of AT2018hyz to constrain the model parameters for both scenarios. While the parameters can be estimated using the equipartition analysis, this method does not account for the temporal evolution. As a result, the inferred parameters do not necessarily reproduce the observed time-dependent behavior. We therefore independently determine parameter sets based on our forward modeling, although they do not significantly deviate from those inferred from the equipartition analysis. In this paper, we do not attempt to determine the best-fitting parameters; instead, we search for parameter sets that reasonably reproduce the observations.

3.1.1. Delayed Outflow Scenario

Figure 2 depicts the radio light curve at 5 GHz and spectra for different epochs. The adopted parameters are shown in Table 1, and they are obtained by manually varying each value around those inferred from the equipartition analysis to give reasonable fits. We assume that the outflow is spherical and launched at 700 days since the optical discovery as suggested by the previous studies (Y. Cendes et al. 2022, 2025). Although our calculations are based on numerical integration over the jet surface, the results can be largely described by analytical expressions (T. Matsumoto & T. Piran 2021, 2024).²

² In the following analytical argument, we ignore the negligible redshift effect for AT2018hyz ($z = 0.0457$). In particular, for the Newtonian delayed outflow the lab and observer time are effectively identical, $t \simeq T$.

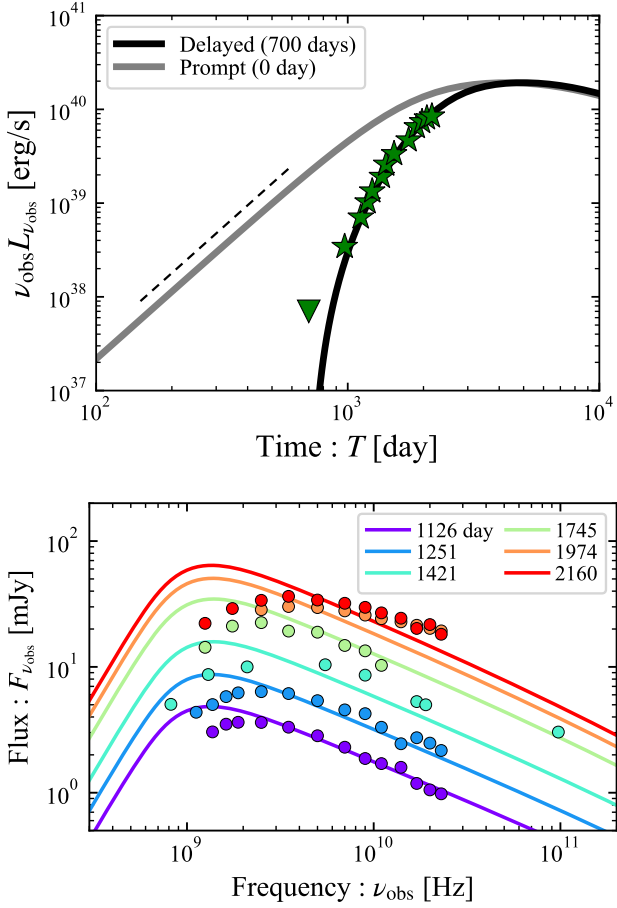


Figure 2. The radio light curve and spectrum of AT2018hyz for the delayed outflow model. (**Top**) The 5 GHz light curve. The black and gray curves show the model light curves of a spherical outflow launched at $T = 700$ (delayed) and 0 day (prompt), respectively. The black dashed line represents the analytical scaling of the flux, $F_\nu \propto T^{\frac{12-k(p+5)}{4}}$. (**Bottom**) The radio spectrum at each epoch. Solid curves show the model spectra corresponding to the black curve in the top panel.

The sharp rise in the light curve is caused by the offset in the origin of time. In this phase, the 5 GHz band is optically thin (see the bottom panel of Fig. 2), and hence the increase in flux results from accumulation of emitting electrons swept up by the freely coasting outflow, which is given by $F_\nu \propto R^{\frac{12-k(p+5)}{4}}$ (Eq. 8). The gray curve shows the light curve from a promptly launched outflow, which agrees with the above scaling. Therefore for given p and T_0 , the light-curve slope constrains the slope of the density profile, k . The flux peaks when the outflow begins decelerating.

In contrast to the light curve, obtaining reasonable spectral fits is challenging, particularly in the optically thick, low-frequency regime. Observations find the peak frequency staying around $\simeq 3$ GHz (Y. Cendes et al.

2025), whereas our result gives a slightly lower value of $\simeq 1$ GHz. While the peak is rounded, it could be interpreted as being shaped by SSA whose peak flux F_{ν_a} and frequency ν_a are given by (T. Matsumoto & T. Piran 2021)

$$F_{\nu_a} \propto \left[\varepsilon_e^{5(p-1)} \varepsilon_B^{\frac{2p+3}{2}} n^{\frac{2p+13}{2}} R^{2p+13} \beta^{\frac{12p-7}{2}} \right]^{\frac{1}{p+4}} \quad (17)$$

$$\propto^{p=2.2} \varepsilon_e^{0.97} \varepsilon_B^{0.60} n^{1.4} \beta^{4.4},$$

$$\nu_a \propto \left[\varepsilon_e^{2(p-1)} \varepsilon_B^{\frac{p+2}{2}} n^{\frac{p+6}{2}} R^2 \beta^{5p-2} \right]^{\frac{1}{p+4}} \quad (18)$$

$$\propto^{p=2.2} \varepsilon_e^{0.39} \varepsilon_B^{0.34} n^{0.66} \beta^{1.8}.$$

Both flux and frequency increase with the parameters, but the flux exhibits a stronger dependence than the frequency. This makes it difficult to increase the frequency by naively changing the parameters with fixing the flux. Since detailed fitting is not the purpose of this paper and the SSA frequency also depends on the outflow geometry, we do not pursue the discrepancy further.

Our resulting energy $E_{ej} = 10^{52}$ erg is $\simeq 50$ times larger than the equipartition estimate by Y. Cendes et al. (2025). However, the discrepancy is not a serious issue because the equipartition analysis measures only the energy in the shocked and radio emitting region, which can be smaller for freely coasting outflows (T. Matsumoto et al. 2022). In addition, such a large energy can also be inferred from the observational indication that the outflow remains in a free-expansion phase at the latest observation, $\simeq 2000$ days. Assuming a constant CNM profile, the deceleration time is given by

$$T_{dec} \simeq \left(\frac{3E_{ej}}{2\pi m_p c^5 n \beta_0^5} \right)^{1/3}. \quad (19)$$

Since the deceleration effect appears a little earlier than T_{dec} , say half of the timescale, we may infer the timescale longer than $\simeq 2 \times (2000 - 700) = 2600$ days, where we account for the shift of 700 days in the time origin. Then we obtain a lower limit on the energy by $T_{dec} \gtrsim 2600 + 700 = 3300$ days, as

$$E_{ej} \gtrsim 5.8 \times 10^{51} \text{ erg} \left(\frac{n}{1 \text{ cm}^{-3}} \right) \left(\frac{\beta_0}{0.3} \right)^5 \left(\frac{T}{3300 \text{ day}} \right)^3. \quad (20)$$

Here the density is motivated by our resulting profile and the size of the outflow.

We comment on the value of our $\varepsilon_B = 0.1$ larger than that of Y. Cendes et al. (2025), $\sim 10^{-3}$, who used an X-ray upper limit. Our synchrotron flux does not violate the limit. This is because we fix $p = 2.2$ for entire our calculation while Y. Cendes et al. (2025) adopt $p < 2$, which is inferred by their spectral fit.

Table 1. Model Parameters of AT2018hyz for the Delayed Outflow and Off-axis Jet Scenarios.

Symbol	Parameter	Delayed Outflow	Off-axis Jet
θ_j	Half opening angle	π	0.1 rad
β_0	Initial velocity	0.25	-
Γ_0	Initial Lorentz factor	-	30
E_{ej}	Kinetic energy	10^{52} erg	10^{56} erg
\tilde{n}	Normalization of CNM density profile at 3×10^{17} cm	8 cm^{-3}	2 cm^{-3}
k	Slope of CNM density profile	1/3	0
p	Slope of electron distribution	2.2	2.2
ε_e	Energy fraction of non-thermal electron energy	0.3	0.07
ε_B	Energy fraction of magnetic field	0.1	0.001
T_0	Outflow launch time	700 day	0 day

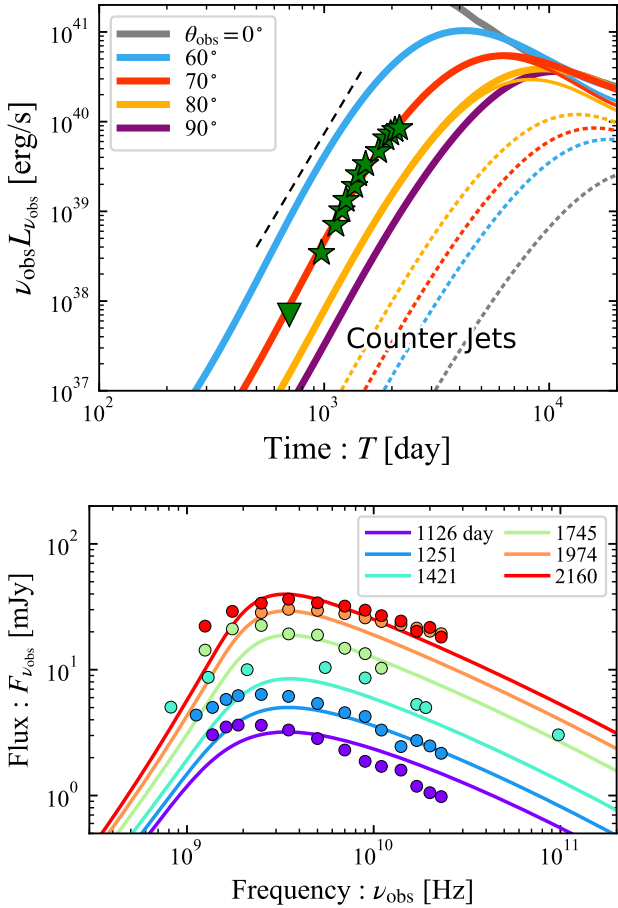


Figure 3. The same as Fig. 2 but for the off-axis jet model with different viewing angles. (**Top**) The thick solid curves show the total radio luminosity contributed by both approaching (thin solid) and counter (dotted) jets while the former almost overlaps with the thick solid curves for $\lesssim 10000$ days. The black dashed line represents the analytical scaling, $F_\nu \propto T^{\frac{3(5-p)}{2}}$. (**Bottom**) The solid curves denote the model spectra corresponding to $\theta_{\text{obs}} = 70^\circ$.

3.1.2. Off-axis Jet Scenario

Figure 3 depicts the radio light curve and spectrum calculated for the off-axis jet model. The adopted parameters are chosen in the same way as in the delayed outflow model and shown in Table 1. The light curves rise rapidly as the jet decelerates and weakens the off-axis effect. The radio flux is larger for smaller viewing angles, and the contribution of the counter jet is completely negligible unless $\theta_{\text{obs}} \gtrsim 80^\circ$, until the light curves peak. The peak is reached when the jet becomes Newtonian $\Gamma \simeq \delta_D \simeq 1$.

The evolution in the rising phase can be understood analytically. For a viewing angle larger than $\theta_{\text{obs}} \gg \theta_j$ and $1/\Gamma$, the flux is contributed almost equally by the entire jet, so that the one-zone approximation is applicable. The optically-thin synchrotron flux is given from Eq. (8):

$$F_{\nu_{\text{obs}}} \propto \varepsilon_e^{p-1} \varepsilon_B^{\frac{p+1}{4}} n^{\frac{p+5}{4}} R^3 \theta_j^2 \Gamma^{\frac{3p-1}{2}} \delta_D^{\frac{p+5}{2}} . \quad (21)$$

For a relativistic outflow with $R(t) \simeq ct$ viewed from off axis $\mu \ll 1$, the radius is given by (Eq. 11)

$$R \simeq \frac{cT}{1-\mu} . \quad (22)$$

Note that the outflow apparently does not decelerate ($R \propto T$) in the off-axis regime even in the deceleration phase with $\Gamma \propto (E_{ej}/nR^3)^{1/2}$. We take a point on the jet axis as a representative point (hereafter called the jet center), and set $\mu = \cos \theta_{\text{obs}}$. By approximating³ the Doppler factor (Eq. 9) and radius (Eq. 22) as $\delta_D \simeq 2/\Gamma \theta_{\text{obs}}^2$ and $R \simeq 2cT/\theta_{\text{obs}}^2$, and plugging these expressions into Eq. (21) we obtain

$$\begin{aligned} F_{\nu_{\text{obs}}} &\propto \varepsilon_e^{p-1} \varepsilon_B^{\frac{p+1}{4}} n^{\frac{11-p}{4}} T^{\frac{3(5-p)}{2}} E_{ej}^{\frac{p-3}{2}} \theta_j^2 \theta_{\text{obs}}^{2(p-10)} \\ &\stackrel{p=2.2}{\propto} \varepsilon_e^{1.2} \varepsilon_B^{0.8} n^{2.2} E_{ej}^{-0.4} T^{4.2} \theta_j^2 \theta_{\text{obs}}^{-15.6} . \end{aligned} \quad (23)$$

³ We use $1 - \cos \theta_{\text{obs}} \simeq \theta_{\text{obs}}^2/2$, which remains accurate to within 20% even at $\theta = \pi/2$.

The scaling of T agrees with our numerical results (see also P. Beniamini et al. 2023). In this example, $\theta_{\text{obs}} = 70^\circ$ provides the best match to the observations, although there is a degeneracy among parameters as seen in Eq. (23).

The bottom panel of Fig. 3 shows the spectra for $\theta_{\text{obs}} = 70^\circ$. The quality of the fit seems better than the delayed outflow model (Fig. 2), and in particular the spectral peaks are located at $\simeq 3$ GHz. The early-time model spectra ($\lesssim 1400$ days) exhibit a rounded peak in contrast to the later ones. This is because the SSA and synchrotron characteristic frequencies (see Appendix A for the latter's definition), overlap at the early phase, $\nu_a \sim \nu_m$, which is also implied by the equipartition analysis (Y. Cendes et al. 2025). ν_m decreases faster, resulting in a narrow peak shaped only by SSA.

Our model suggests a huge jet energy, $E_{\text{j},\text{iso}} = E_{\text{ej}} \sim 10^{56}$ erg, even after accounting for the beaming correction, $E_{\text{j}} \sim \theta_j^2 E_{\text{j},\text{iso}} \sim 10^{54}$ erg. This value comes from two conditions. One is that the jet should be decelerating at the detection of the radio flare, $T \sim 1000$ day:

$$E_{\text{ej}} \lesssim \frac{4\pi}{3} m_p c^2 n \Gamma^2 R^3 \simeq 8.8 \times 10^{55} \text{ erg} \\ \times \left(\frac{n}{1 \text{ cm}^{-3}} \right) \left(\frac{\Gamma}{10} \right)^2 \left(\frac{T}{1000 \text{ day}} \right)^3 \theta_{\text{obs}}^{-6}, \quad (24)$$

where we used $R \simeq 2cT/\theta_{\text{obs}}^2$. The other comes from the fact that the jet should be still relativistic at the latest observation $T \simeq 2000$ day, since the observed light curve is still rising and has not yet reached its peak. This sets a lower limit on the jet energy:

$$E_{\text{ej}} \gtrsim \frac{4\pi}{3} m_p c^2 n (cT)^3 \\ \simeq 8.7 \times 10^{53} \text{ erg} \left(\frac{n}{1 \text{ cm}^{-3}} \right) \left(\frac{T}{2000 \text{ day}} \right)^3. \quad (25)$$

This implied energy is near the maximum of allowed energetics for normal TDEs. However, such powerful jets are also implied by radio modeling of other events (e.g., E. Berger et al. 2012; T. Matsumoto & B. D. Metzger 2023).

3.2. Image

Figure 4 shows the synthetic radio intensity maps at 5 GHz calculated for the delayed outflow (left) and off-axis jet (right) scenarios. The parameters are the same as ones used in the calculations for the light curves and spectra. In each map, the surface brightness is normalized to the upper 95% of the distribution, and values exceeding the 95th percentile are clipped to that percentile level. For AT2018hyz with $z = 0.0457$, the angular diameter distance is $d_A \simeq 186.5$ Mpc, and hence the angular size is $\hat{X} \simeq 3.6$ mas ($X/10^{19}$ cm). At 5 GHz, the entire emitting region in both scenarios is optically thin.

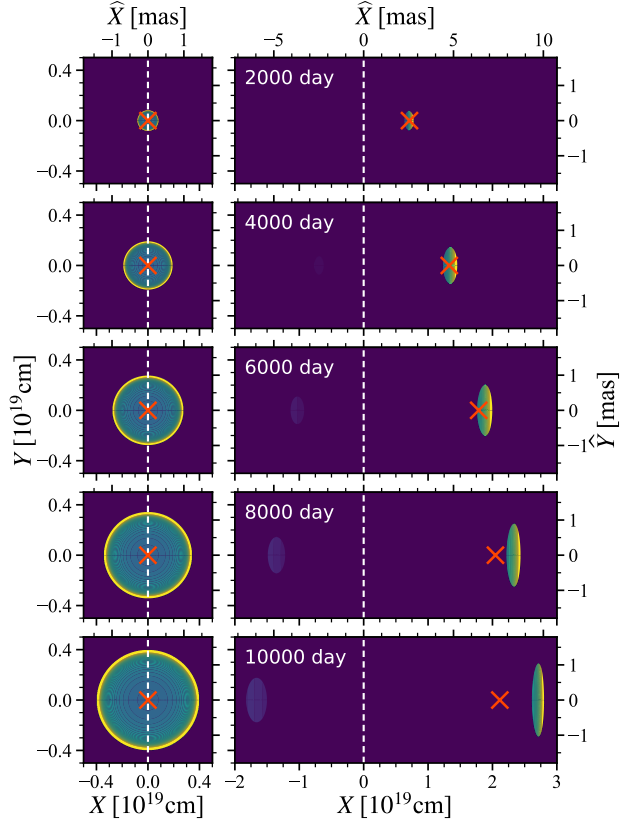


Figure 4. The synthetic radio intensity maps of AT2018hyz at 5 GHz for the delayed outflow (left) and off-axis jet models (right). In each panel, the left and bottom axes represent the physical distance, while the right and top ones represent the corresponding angular distance. The red crosses show the location of the emission centroid.

The left column of Fig. 4 shows the time evolution of the radio image for the delayed outflow. With the spherical geometry, the outflow appears disk-like on the sky and expands at a constant speed before the deceleration time. After $\simeq 4000$ days, the deceleration becomes significant and the disk grows more slowly in size. Since the emissivity is distributed uniformly over the shock surface, the brightness distribution is described by

$$I_{\nu_{\text{obs}}} \propto \frac{1}{|\mu|} = \frac{1}{\sqrt{1 - (\varpi/R)^2}}, \quad (26)$$

where $\varpi^2 = X^2 + Y^2$. This explains the limb brightening of the images. For frequencies lower than ν_a , the brightness distribution is uniform since $\tau_\nu \propto 1/|\mu|$ (see Eq. 15).

The right column of Fig. 4 shows the images of the off-axis jet. Initially the approaching jet dominates the emission and it moves toward $X > 0$ on the sky. Around $\simeq 6000$ days, the jet becomes Newtonian producing the light curve peak, and the counter jet emerges gradually after that. The intensity is higher for the right side of

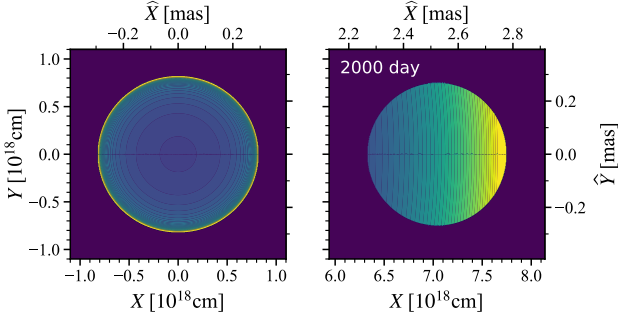


Figure 5. The same as Fig. 4 but the X and Y -axes in both panels are set to equal scales, ensuring that circles are displayed without distortion. The right panel shows only the approaching jet. The intensity normalization in this figure is the upper 99% of the distribution.

the approaching-jet image because a ray can intersect more fluid elements (same as the limb brightening of the delayed outflow).

The jet image is an elliptical disk. However, interestingly, at an early phase $\lesssim 2000$ days the approaching jet has a filled-disk shape like the delayed outflow (see Fig. 5 whose axes have equal scales). This is because the emitting region (the EATS) has a characteristic shape, which is described by an intersection between an egg-shaped EATS of a spherically symmetric relativistic outflow (R. Sari 1998; J. Granot et al. 1999), and the jet geometry. We will show that the aspect ratio of the image is unity in Sec. 4. While the shapes of both delayed outflow and off-axis jet images are identical in this phase, the intensity distributions are different.

The angular resolution of global VLBI is typically $\sim \lambda_{5\text{GHz}}/10000 \text{ km} \simeq \text{mas}$, where $\lambda_{5\text{GHz}} = 6 \text{ cm}$. This implies that, for AT2018hyz, it may be difficult to obtain a resolved image or to detect any substructure. Instead one can detect only an emission centroid as a point source. The emission centroid of each image is calculated by Eq. (16) and shown in Fig. 4 as a red cross.

For the delayed outflow with the spherical symmetry, by definition the centroid stays at the origin. Even if the outflow has a more complicated geometry, the motion of the centroid is Newtonian and limited within an extent of $\lesssim (c\beta)T$. This limit should remain valid even for an outflow with multiple components. In such a case, different components may dominate the emission at different moments, and the emission centroid may track the brightest region and thus exhibit an apparent velocity exceeding $c\beta$. However, the centroid position itself is always confined within a distance $\lesssim (c\beta)T$ from the origin.

For the off-axis jet, the centroid traces the approaching jet until the counter jet starts contributing to the emission. Then the centroid moves backward and eventually returns to the origin. Most importantly, in the early phase the jet is relativistic and the centroid ex-

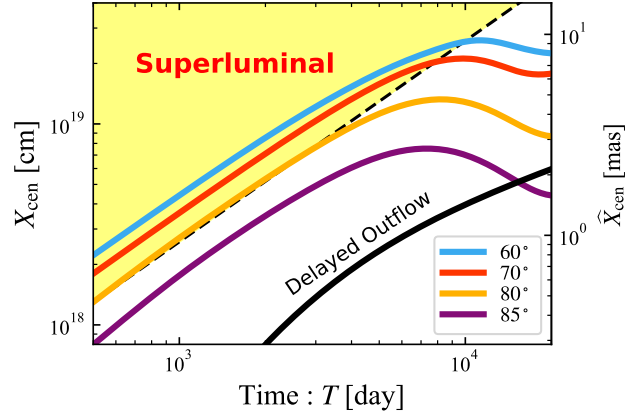


Figure 6. The evolution of the emission centroid of off-axis jets with different viewing angles. The yellow shaded region represents the distance accessible only for a superluminal emission source ($X_{\text{cen}} \geq cT$). The black curve shows the radial size of the delayed outflow.

hibits superluminal motion with an apparent velocity of (e.g., M. J. Rees 1966)

$$\beta_{\text{app}} = \frac{\beta \sin \theta_{\text{obs}}}{1 - \beta \cos \theta_{\text{obs}}} . \quad (27)$$

Figure 6 depicts the time evolution of the emission centroid for the off-axis jet. For a fixed jet velocity, the apparent velocity increases for a smaller viewing angle up to $\theta_{\text{obs}} = 1/\Gamma$. In addition, a smaller θ_{obs} delays the emergence of the counter-jet (see Fig. 3), sustaining the superluminal motion longer. On the other hand, for larger θ_{obs} , the contribution from the counter-jet is no longer negligible, which makes the motion of the centroid subluminal and indistinguishable from that of a Newtonian outflow. The critical viewing angle above which $X_{\text{cen}} \lesssim cT$, can be derived from Eq. (21). In contrast to Eq. (23), without adopting the approximation of $1 - \cos \theta_{\text{obs}} \simeq \theta_{\text{obs}}^2/2$, we obtain the angular dependence of $F_{\nu_{\text{obs}}} \propto (1 - \cos \theta_{\text{obs}})^{p-10} = (1 - \vartheta)^{p-10}$, where $\vartheta \equiv \pi/2 - \theta_{\text{obs}} \ll 1$. Noting the radius of the jet center is given by Eq. (22), one can obtain the location of the emission centroid by a flux-weighted mean of the position of both sided jets:

$$X_{\text{cen}} = \frac{cT}{2} [\sin \theta_{\text{obs}} (1 - \vartheta)^{p-11} - \sin \theta_{\text{obs}} (1 + \vartheta)^{p-11}] \simeq (11 - p)\vartheta cT . \quad (28)$$

We approximate $\sin \theta_{\text{obs}} \simeq 1$ in the second equality. By requiring $X_{\text{cen}} < cT$, the critical angle is given by $(11 - p)\vartheta < 1$, or equivalently

$$\theta \gtrsim \frac{\pi}{2} - \frac{1}{11 - p} \stackrel{p=2.5}{\simeq} 83^\circ , \quad (29)$$

which roughly agrees with our result. While the apparent velocity is Newtonian for larger θ_{obs} , the centroid

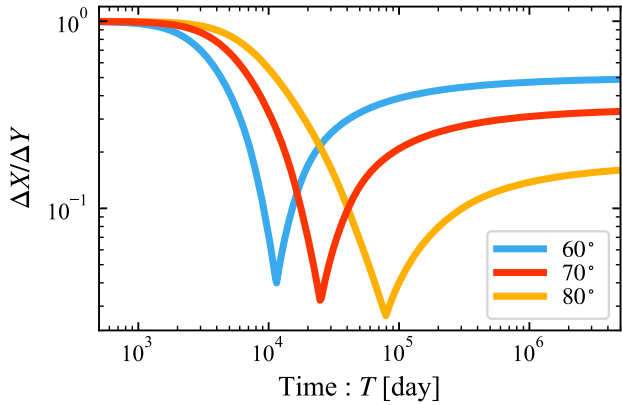


Figure 7. The long-time evolution of the aspect ratio of the approaching jet image for different viewing angles.

should move backward at some point, allowing distinction from the delayed Newtonian outflow.

4. VERY LONG-TIME EVOLUTION

In the previous section, we focused on AT2018hyz and its evolution up to $\sim 10^4$ days ($\simeq 30$ yrs). Over longer timescales, the jet image also exhibits several interesting behaviors. Although such a long timescale exceeds the period over which a single human researcher can work, it may be possible to observe the same phenomena in a shorter timescale for less energetic events such as other off-axis jetted TDEs with lower energy and Galactic microquasars.

The shape of the off-axis approaching jet image shows a characteristic evolution reflecting its dynamics. Figure 7 depicts the long-time evolution of the aspect ratio of the image defined as the ratio of the image widths in the X and Y directions. Initially the image is a disk with an aspect ratio of unity as seen in Fig. 5, but it decreases with time, meaning that the image is elongated in the Y direction (see the lower panels in Fig. 4). Afterward, the ratio reaches a minimum at $\sim 10^{4-5}$ days, then starts to increase, and eventually approaches a constant value. This behavior results from the deceleration of the jet from relativistic to Newtonian motion, which alters the geometry of the EATS.

Figure 8 illustrates a schematic picture of the evolution of the EATS. The EATS is given by the intersection of the EATS of a spherical outflow (gray curves) and the jet (shaded region). For a relativistic outflow, the former has an egg-like shape, with its broader end oriented toward the observer (R. Sari 1998; J. Granot et al. 1999). In this configuration, the far and near sides of the jet edge (black dots) are projected to smaller and larger X -coordinates, which we denote as X_{\min} and X_{\max} , respectively. In contrast, the EATS of a spherical Newtonian outflow is simply spherical. In this case, the far and near sides are projected to larger and smaller X -coordinates in the image, respectively. Therefore, as the jet decel-

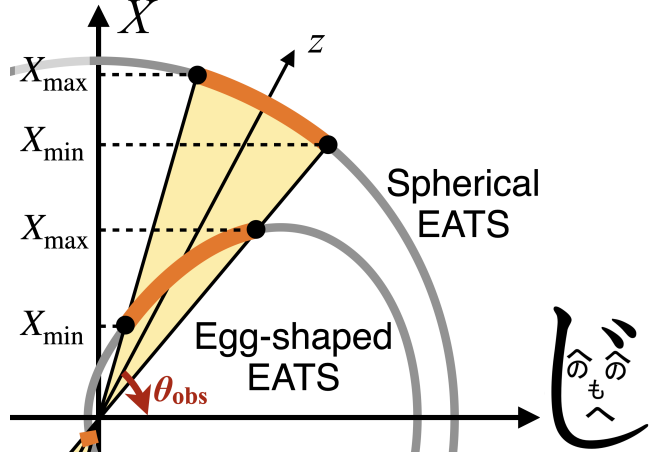


Figure 8. A schematic picture of the EATS of the off-axis jet at relativistic and Newtonian regimes. The EATS is given by the intersection of that of a spherical outflow (gray curves) and the jet (shaded region). In the relativistic phase, the former has an egg-like shape, and the far and near sides of the jet edge (black dots) are projected to smaller and larger X coordinates on the sky plane, which we denote as X_{\min} and X_{\max} , respectively. In the Newtonian phase, the far (near) side is projected to X_{\max} (X_{\min}).

erates, the projected locations of the far and near sides of the jet edge flip on the sky plane, and the width ΔX has a minimum.

We derive the expressions of the aspect ratio in both relativistic and Newtonian limits. The width in the Y direction is simply given by $\Delta Y = 2R_j \sin \theta_{\text{obs}} \sin \theta_j \simeq 2R_j \theta_j$, where R_j is the radius of the jet center and given by Eq. (22) with $\mu = \cos \theta_{\text{obs}}$. In the relativistic limit, the points X_{\min} and X_{\max} correspond to the far and near sides of the jet, respectively. Their radii are also given by Eq. (22) with $\mu = \cos(\theta_{\text{obs}} \pm \theta_j)$, where the plus (minus) sign corresponds to the far (near) side of the jet. Multiplying them by $\sin(\theta_{\text{obs}} \pm \theta_j)$ to project on the sky plane, the width in the X direction is given by

$$\Delta X = X_{\max} - X_{\min} \simeq 2R_j \theta_j . \quad (30)$$

In the Newtonian limit, the EATS is a sphere and a simple geometrical argument gives

$$\Delta X = 2R_j \theta_j \cos \theta_{\text{obs}} . \quad (31)$$

In summary, the asymptotic value of the aspect ratio is

$$\frac{\Delta X}{\Delta Y} \simeq \begin{cases} 1 & : \text{Relativistic}, \\ \cos \theta_{\text{obs}} & : \text{Newtonian}. \end{cases} \quad (32)$$

The time at which the ratio takes the minimum is estimated as a conjunction point of radii of the jet center in both limits. The latter is roughly given by the energy

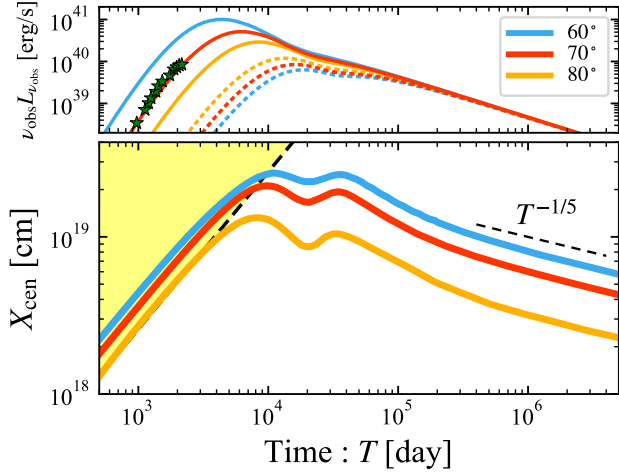


Figure 9. The long time evolution of the radio luminosity at 5 GHz (top), and the location of the emission centroid (bottom) for various viewing angles.

conservation:

$$R(T) = \left(\frac{75E_{\text{ej}}}{8\pi m_p n} T^2 \right)^{1/5}. \quad (33)$$

By equating them one can derive the timescale

$$T_{\min} \simeq 2.3 \times 10^4 \text{ day} \left(\frac{n}{1 \text{ cm}^{-3}} \right)^{-1/3} \left(\frac{E_{\text{ej}}}{10^{56} \text{ erg}} \right)^{1/3} (1 - \cos \theta_{\text{obs}})^{5/3}. \quad (34)$$

In addition to the image, the location of the emission centroid also shows a characteristic evolution. As we discussed in Sec. 3.2, the centroid comes back to the origin as the luminosities of both jets become comparable at late time. Counterintuitively, this happens not instantaneously but gradually as shown in Fig. 9. The centroid reaches a maximum in the X coordinate at $\sim 10^4$ days (see also Fig. 6), exhibits a shallow dip, and then *slowly* returns toward the origin. The dip corresponds to the transition into the deep Newtonian phase (Y. F. Huang & K. S. Cheng 2003; L. Sironi & D. Giannios 2013), during which the luminosity from the approaching jet begins to decline more slowly, temporarily reducing the relative contribution from the counter jet. Once the counter jet enters the deep Newtonian phase, the two jets become nearly symmetric for $T \gtrsim 10^5$ days.

Naively, one might expect the centroid to return to the origin shortly after the brightness symmetry is established. However, in practice the recession follows a power-law in T , because a small optical path difference exists. For photons to arrive at an observer at T , they should be emitted from the approaching and counter jets at

$$R_{j,\text{ap}} = \frac{c\beta T}{1 \mp \beta \cos \theta_{\text{obs}}}, \quad (35)$$

where the subscripts “ap” and “co” denote the approaching and counter jets, respectively. It should be noted that different from Eq. (22), the velocity β is necessary in the Newtonian limit. In short, the photons from the counter jet should be emitted earlier to compensate the traveling time for the path difference and be received at T . This means the counter jet is closer to the origin than the approaching jet. The location of the centroid is given by

$$X_{\text{cen}} \simeq \sin \theta_{\text{obs}} R_{j,\text{ap}} - \sin \theta_{\text{obs}} R_{j,\text{co}} \propto \beta^2 T, \quad (36)$$

where $\beta \cos \theta_{\text{obs}} \ll 1$. Although the above argument assumes a constant velocity and equal luminosities from both jets, the scaling is generally valid in the Newtonian regime. In the deceleration phase, $\beta \propto T^{-3/5}$, yielding $X_{\text{cen}} \propto T^{-1/5}$ consistent with our result (Fig. 9). That being discussed, in the case of jetted TDEs, both jets may be resolved into two distinct sources at such late time due to a large separation. Therefore, the above discussion may be meaningful for more compact sources such as microquasars.

Finally, we note a caveat regarding the above results. We calculated the jet image at very late time under the assumption that the jet keeps its original top-hat geometry and does not experience a side-way expansion. This may be a good approximation for TDEs with powerful jets until the trans-relativistic phase, but may not be justified in the Newtonian phase. However, our findings, the evolution of the aspect ratio and the gradually receding emission centroid, could remain unchanged. In the former result, the ratio takes the minimum in the trans-relativistic phase, and for the latter one, the optical path difference still exists regardless of the jet geometry. In addition, we note recent hydrodynamical simulations find a Newtonian conical outflow expands almost keeping its original geometry (e.g., G. Mou 2025).

5. SUMMARY

The origin of late-time radio flares in TDEs remains uncertain. Among these events, the radio flare associated with AT2018hyz is particularly enigmatic, exhibiting an unprecedentedly sharp and sustained rise and a luminosity comparable to those of jetted TDEs (Y. Cendes et al. 2022; I. Sfaradi et al. 2024; Y. Cendes et al. 2025). The leading scenarios for the radio flare of AT2018hyz involve either an interaction between the CNM and a delayed outflow launched approximately 1000 days after the optical discovery, or an off-axis jet launched around the time of discovery but oriented away from our line of sight. Analyses based on the radio light curve and spectrum alone have difficulty distinguishing between these two scenarios. Radio imaging with VLBI therefore provides the most direct diagnostics to break this degeneracy (T. Matsumoto & T. Piran 2023).

In this paper, we synthesize radio images for both scenarios. In the delayed outflow scenario, the radio image

directly reflects the geometry of the outflow. In our case, a spherical outflow produces a disk-like image. The characteristic size is set by the radial extent of the outflow, $\sim (c\beta)T$, and increases linearly with time until significant deceleration occurs. In this geometry, the emission centroid remains stationary at the origin. Even if the outflow deviates from spherical symmetry and consists of multiple components, the centroid motion is confined within a similar range of $\lesssim (c\beta)T$.

In the off-axis jet scenario, the radio image is initially dominated by the approaching jet, and most importantly, the emission centroid exhibits superluminal motion, which would be a smoking-gun signature of a relativistic jet. As the jet decelerates, the counter-jet begins to contribute to the emission, and the centroid gradually returns toward the origin. At early times, the image of the approaching jet has a disk-like shape, similar to that of a spherical delayed outflow, but it later becomes elongated in the direction perpendicular to the jet motion. The aspect ratio of the image reaches a minimum and then increases, asymptotically approaching a constant value. This non-monotonic evolution reflects the changing geometry of the EATS. We note that these results for off-axis jets should also apply to other astrophysical systems, such as microquasars and gamma-ray bursts.

Thus far, we have focused on radio VLBI observations, which provide the most direct way to resolve the source structure. However, if one is interested only in the loca-

tion of the emission centroid rather than resolving the image, precise astrometry may also be achieved with optical or infrared (IR) telescopes, as demonstrated for GW170817 with *HST* (K. P. Mooley et al. 2022). Although the diffraction limit of ~ 100 mas prevents direct imaging of the source structure, the emission centroid can still be determined with high precision, provided that the source is sufficiently bright. For AT2018hyz with $p \simeq 2.2$, the optical/IR luminosity may be comparable to that in the radio band, $\sim 10^{40}$ erg s $^{-1}$. In the crowded nuclear region of the host galaxy, contamination from stellar light is expected to be severe in the optical band, making IR observations more suitable. If the synchrotron afterglow outshines the surrounding stellar emission, the position of the point source could be measured and potentially used to confirm superluminal motion with facilities such as *JWST*.

ACKNOWLEDGEMENTS

We thank Yvette Cendes for fruitful discussions on late-time radio observations, and Kazuya Takahashi for motivating the author to initiate this work. We are also grateful to Kenta Hotokezaka and Jonathan Granot for stimulating discussions. This research is supported by JSPS KAKENHI (grant No. 24K17088).

APPENDIX

A. SYNCHROTRON EMISSION

This Appendix summarizes the basic ingredients required to compute the synchrotron emissivity and absorption coefficient. We follow the standard synchrotron emission model (R. Sari et al. 1998), extending it to smoothly connect the relativistic and Newtonian regimes. Following the passage of the shock, the particle number and internal energy densities are determined by the shock jump conditions:

$$n' \simeq 4\Gamma n \quad \text{and} \quad e'_{\text{in}} \simeq m_p c^2 (\Gamma - 1) n'. \quad (\text{A1})$$

Assuming fractions ε_B and ε_e of the internal energy are converted to the energies of the magnetic field and non-thermal electrons, respectively, one obtains the magnetic field

$$B' \simeq (8\pi\varepsilon_B e'_{\text{in}})^{1/2}, \quad (\text{A2})$$

and the minimum Lorentz factor of electrons

$$\gamma_m = \varepsilon_e \left(\frac{p-2}{p-1} \right) \frac{m_p}{m_e} (\Gamma - 1), \quad (\text{A3})$$

where m_e is the electron mass, and the electrons have a power-law distribution, $dn_e/d\gamma \propto \gamma^{-p}$. For outflows

with a lower velocity

$$\beta < \beta_{\text{DN}} \equiv \left[\frac{4}{\varepsilon_e} \left(\frac{p-1}{p-2} \right) \frac{m_e}{m_p} \right]^{1/2} \stackrel{p=2.2}{\simeq} 0.21 \left(\frac{\varepsilon_e}{0.3} \right)^{-1/2}, \quad (\text{A4})$$

Eq. (A3) yields an unphysical value, $\gamma_m \lesssim 1$. In this deep-Newtonian phase we fix $\gamma_m = 2$ and multiply n' in Eqs. (A8) and (A9) by a factor $f_{\text{DN}} \equiv (\beta/\beta_{\text{DN}})^2$ (T. Matsumoto & T. Piran 2021).

The synchrotron frequency and emissivity of single electron with γ are given by

$$\nu'(\gamma) = \frac{\gamma^2 e B'}{2\pi m_e c} \quad \text{and} \quad P'(\gamma) = \frac{4}{3} \sigma_T c \gamma^2 \frac{(B')^2}{8\pi}, \quad (\text{A5})$$

respectively, where e and σ_T are the elementary charge and Thomson cross section, respectively. The critical Lorentz factor above which electrons are under fast cooling, is given by equating the electron's energy $\gamma_c m_e c^2$ and emitted energy during a dynamical timescale $P'(\gamma_c) t'$:

$$\gamma_c = \frac{6\pi m_e c}{\sigma_T (B')^2 t'}, \quad (\text{A6})$$

where $t' = t/\Gamma$ is the dynamical time in the fluid rest frame. Then the synchrotron emissivity in the slow cooling regime ($\gamma_m < \gamma_c$) is given by

$$j'_{\nu'} = (j'_{\nu'})_{\text{peak}} \begin{cases} \left(\frac{\nu'}{\nu'_m}\right)^{1/3} & : \nu' < \nu'_m , \\ \left(\frac{\nu'}{\nu'_m}\right)^{\frac{1-p}{2}} & : \nu'_m < \nu' < \nu'_c , \\ \left(\frac{\nu'_c}{\nu'_m}\right)^{\frac{1-p}{2}} \left(\frac{\nu'}{\nu'_m}\right)^{-\frac{p}{2}} & : \nu'_c < \nu' , \end{cases} \quad (\text{A7})$$

where $\nu'_m = \nu'(\gamma_m)$, $\nu'_c = \nu'(\gamma_c)$, and

$$(j'_{\nu'})_{\text{peak}} = \frac{n'(P'/\nu')}{4\pi} = \frac{\sigma_T m_e c^2 n' B'}{12\pi e} . \quad (\text{A8})$$

The absorption coefficient is given by the standard formula in G. B. Rybicki & A. P. Lightman (1979) (their Eq. 6.50). For an electron population with a single power-law distribution, it can be written as

$$\alpha'_{\nu'} = \frac{(p+2)(p-1)\sqrt{3}e^3 n' B'}{16\pi m_e^2 c^2 \gamma_m (\nu')^2} \left(\frac{\nu'}{\nu'_m}\right)^{-p/2} I_p(\nu'/\nu'_m) , \quad (\text{A9})$$

where

$$I_p(x) \equiv \int_0^x dy y^{\frac{p-2}{2}} F(y) \quad (\text{A10})$$

$$\simeq \begin{cases} \frac{2^{\frac{p+2}{2}}}{p+2} \Gamma\left(\frac{3p+22}{12}\right) \Gamma\left(\frac{3p+2}{12}\right) : x \gg 1 , \\ \frac{2^{8/3} 3^{1/2} \pi}{(3p+2)\Gamma(1/3)} x^{\frac{3p+2}{6}} : x \ll 1 , \end{cases}$$

$$F(x) \equiv x \int_x^\infty K_{5/3}(y) dy , \quad (\text{A11})$$

where $\Gamma(x)$ and $K_{5/3}(x)$ are the Gamma function and modified Bessel function, respectively. We remark that G. B. Rybicki & A. P. Lightman (1979) originally obtain the absorption coefficient (their Eq. 6.53) in the limit of $\nu \gg \nu_m$ keeping the dependence on the electron pitch angle θ_p and adopting a slightly different definition of the characteristic frequency, $\nu'(\gamma) = 3\gamma^2 eB' \sin \theta_p / 4\pi m_e c$, instead of our Eq. (A5). Their equation is identical to ours by introducing ν_m and setting $\sin \theta_p \rightarrow 1$.

REFERENCES

- Alexander, K. D., Margutti, R., Gomez, S., et al. 2025, arXiv e-prints, arXiv:2506.12729, doi: [10.48550/arXiv.2506.12729](https://doi.org/10.48550/arXiv.2506.12729)
- Barniol Duran, R., Nakar, E., & Piran, T. 2013, ApJ, 772, 78, doi: [10.1088/0004-637X/772/1/78](https://doi.org/10.1088/0004-637X/772/1/78)
- Beniamini, P., Piran, T., & Matsumoto, T. 2023, MNRAS, 524, 1386, doi: [10.1093/mnras/stad1950](https://doi.org/10.1093/mnras/stad1950)
- Berger, E., Zauderer, A., Pooley, G. G., et al. 2012, ApJ, 748, 36, doi: [10.1088/0004-637X/748/1/36](https://doi.org/10.1088/0004-637X/748/1/36)
- Bruni, G., O'Connor, B., Matsumoto, T., et al. 2021, MNRAS, 505, L41, doi: [10.1093/mnrasl/slab046](https://doi.org/10.1093/mnrasl/slab046)
- Cendes, Y., Eftekhari, T., Berger, E., & Polisensky, E. 2021, ApJ, 908, 125, doi: [10.3847/1538-4357/abd323](https://doi.org/10.3847/1538-4357/abd323)
- Cendes, Y., Berger, E., Alexander, K. D., et al. 2022, ApJ, 938, 28, doi: [10.3847/1538-4357/ac88d0](https://doi.org/10.3847/1538-4357/ac88d0)
- Cendes, Y., Berger, E., Alexander, K. D., et al. 2024, ApJ, 971, 185, doi: [10.3847/1538-4357/ad5541](https://doi.org/10.3847/1538-4357/ad5541)
- Cendes, Y., Berger, E., Beniamini, P., et al. 2025, arXiv e-prints, arXiv:2507.08998, doi: [10.48550/arXiv.2507.08998](https://doi.org/10.48550/arXiv.2507.08998)
- Christy, C. T., Alexander, K. D., Margutti, R., et al. 2024, ApJ, 974, 18, doi: [10.3847/1538-4357/ad675b](https://doi.org/10.3847/1538-4357/ad675b)
- Eftekhari, T., Berger, E., Zauderer, B. A., Margutti, R., & Alexander, K. D. 2018, ApJ, 854, 86, doi: [10.3847/1538-4357/aaa8e0](https://doi.org/10.3847/1538-4357/aaa8e0)
- Fender, R. 2006, in Compact stellar X-ray sources, ed. W. H. G. Lewin & M. van der Klis, Vol. 39, 381–419, doi: [10.48550/arXiv.astro-ph/0303339](https://doi.org/10.48550/arXiv.astro-ph/0303339)
- Fernández, J. J., Kobayashi, S., & Lamb, G. P. 2022, MNRAS, 509, 395, doi: [10.1093/mnras/stab2879](https://doi.org/10.1093/mnras/stab2879)
- Ghirlanda, G., Salafia, O. S., Paragi, Z., et al. 2019, Science, 363, 968, doi: [10.1126/science.aau8815](https://doi.org/10.1126/science.aau8815)
- Giannios, D., & Metzger, B. D. 2011, MNRAS, 416, 2102, doi: [10.1111/j.1365-2966.2011.19188.x](https://doi.org/10.1111/j.1365-2966.2011.19188.x)
- Gill, R., & Granot, J. 2018, MNRAS, 478, 4128, doi: [10.1093/mnras/sty1214](https://doi.org/10.1093/mnras/sty1214)
- Golay, W. W., Berger, E., Cendes, Y., et al. 2025, arXiv e-prints, arXiv:2508.16756, doi: [10.48550/arXiv.2508.16756](https://doi.org/10.48550/arXiv.2508.16756)
- Gomez, S., Nicholl, M., Short, P., et al. 2020, MNRAS, 497, 1925, doi: [10.1093/mnras/staa2099](https://doi.org/10.1093/mnras/staa2099)
- Goodwin, A. J., Alexander, K. D., Miller-Jones, J. C. A., et al. 2023, MNRAS, 522, 5084, doi: [10.1093/mnras/stad1258](https://doi.org/10.1093/mnras/stad1258)
- Goodwin, A. J., Mummary, A., Laskar, T., et al. 2025, ApJ, 981, 122, doi: [10.3847/1538-4357/adb0b1](https://doi.org/10.3847/1538-4357/adb0b1)
- Govreen-Segal, T., & Nakar, E. 2023, MNRAS, 524, 403, doi: [10.1093/mnras/stad1628](https://doi.org/10.1093/mnras/stad1628)
- Granot, J., De Colle, F., & Ramirez-Ruiz, E. 2018, MNRAS, 481, 2711, doi: [10.1093/mnras/sty2454](https://doi.org/10.1093/mnras/sty2454)

- Granot, J., & Piran, T. 2012, MNRAS, 421, 570, doi: [10.1111/j.1365-2966.2011.20335.x](https://doi.org/10.1111/j.1365-2966.2011.20335.x)
- Granot, J., Piran, T., & Sari, R. 1999, ApJ, 513, 679, doi: [10.1086/306884](https://doi.org/10.1086/306884)
- Hajela, A., Alexander, K. D., Margutti, R., et al. 2025, ApJ, 983, 29, doi: [10.3847/1538-4357/adb620](https://doi.org/10.3847/1538-4357/adb620)
- Hammerstein, E., van Velzen, S., Gezari, S., et al. 2023, ApJ, 942, 9, doi: [10.3847/1538-4357/aca283](https://doi.org/10.3847/1538-4357/aca283)
- Ho, A. Y. Q., Yao, Y., Matsumoto, T., et al. 2025, ApJ, 989, 54, doi: [10.3847/1538-4357/ade8f2](https://doi.org/10.3847/1538-4357/ade8f2)
- Horesh, A., Cenko, S. B., & Arcavi, I. 2021a, Nature Astronomy, 5, 491, doi: [10.1038/s41550-021-01300-8](https://doi.org/10.1038/s41550-021-01300-8)
- Horesh, A., Sfaradi, I., Fender, R., et al. 2021b, ApJL, 920, L5, doi: [10.3847/2041-8213/ac25fe](https://doi.org/10.3847/2041-8213/ac25fe)
- Hu, F. F., Goodwin, A., Price, D. J., et al. 2025, ApJL, 988, L24, doi: [10.3847/2041-8213/adeb79](https://doi.org/10.3847/2041-8213/adeb79)
- Huang, Y. F., & Cheng, K. S. 2003, MNRAS, 341, 263, doi: [10.1046/j.1365-8711.2003.06430.x](https://doi.org/10.1046/j.1365-8711.2003.06430.x)
- Lu, W., Matsumoto, T., & Matzner, C. D. 2024, MNRAS, 533, 979, doi: [10.1093/mnras/stae1770](https://doi.org/10.1093/mnras/stae1770)
- Matsumoto, T., & Metzger, B. D. 2023, MNRAS, 522, 4028, doi: [10.1093/mnras/stad1182](https://doi.org/10.1093/mnras/stad1182)
- Matsumoto, T., & Piran, T. 2021, MNRAS, 507, 4196, doi: [10.1093/mnras/stab2418](https://doi.org/10.1093/mnras/stab2418)
- Matsumoto, T., & Piran, T. 2023, MNRAS, 522, 4565, doi: [10.1093/mnras/stad1269](https://doi.org/10.1093/mnras/stad1269)
- Matsumoto, T., & Piran, T. 2024, ApJ, 971, 49, doi: [10.3847/1538-4357/ad58ba](https://doi.org/10.3847/1538-4357/ad58ba)
- Matsumoto, T., Piran, T., & Krolik, J. H. 2022, MNRAS, 511, 5085, doi: [10.1093/mnras/stac382](https://doi.org/10.1093/mnras/stac382)
- Mimica, P., Giannios, D., Metzger, B. D., & Aloy, M. A. 2015, MNRAS, 450, 2824, doi: [10.1093/mnras/stv825](https://doi.org/10.1093/mnras/stv825)
- Mirabel, I. F., & Rodríguez, L. F. 1994, Nature, 371, 46, doi: [10.1038/371046a0](https://doi.org/10.1038/371046a0)
- Mooley, K. P., Anderson, J., & Lu, W. 2022, Nature, 610, 273, doi: [10.1038/s41586-022-05145-7](https://doi.org/10.1038/s41586-022-05145-7)
- Mooley, K. P., Deller, A. T., Gottlieb, O., et al. 2018, Nature, 561, 355, doi: [10.1038/s41586-018-0486-3](https://doi.org/10.1038/s41586-018-0486-3)
- Mou, G. 2025, arXiv e-prints, arXiv:2510.14715, doi: [10.48550/arXiv.2510.14715](https://doi.org/10.48550/arXiv.2510.14715)
- Mou, G., & Shu, X. 2025, arXiv e-prints, arXiv:2510.25033, doi: [10.48550/arXiv.2510.25033](https://doi.org/10.48550/arXiv.2510.25033)
- Nedora, V., Dietrich, T., & Shibata, M. 2023, MNRAS, 524, 5514, doi: [10.1093/mnras/stad2128](https://doi.org/10.1093/mnras/stad2128)
- Piran, T., Nakar, E., & Rosswog, S. 2013, MNRAS, 430, 2121, doi: [10.1093/mnras/stt037](https://doi.org/10.1093/mnras/stt037)
- Rees, M. J. 1966, Nature, 211, 468, doi: [10.1038/211468a0](https://doi.org/10.1038/211468a0)
- Rees, M. J. 1988, Nature, 333, 523, doi: [10.1038/333523a0](https://doi.org/10.1038/333523a0)
- Rhoads, J. E. 1999, ApJ, 525, 737, doi: [10.1086/307907](https://doi.org/10.1086/307907)
- Ricci, R., Troja, E., Bruni, G., et al. 2021, MNRAS, 500, 1708, doi: [10.1093/mnras/staa3241](https://doi.org/10.1093/mnras/staa3241)
- Rybicki, G. B., & Lightman, A. P. 1979, Radiative processes in astrophysics
- Sadeh, G., Linder, N., & Waxman, E. 2024, MNRAS, 531, 3279, doi: [10.1093/mnras/stae1286](https://doi.org/10.1093/mnras/stae1286)
- Sari, R. 1998, ApJL, 494, L49, doi: [10.1086/311160](https://doi.org/10.1086/311160)
- Sari, R., Piran, T., & Narayan, R. 1998, ApJL, 497, L17, doi: [10.1086/311269](https://doi.org/10.1086/311269)
- Sato, Y., Murase, K., Bhattacharya, M., et al. 2024, PhRvD, 110, L061307, doi: [10.1103/PhysRevD.110.L061307](https://doi.org/10.1103/PhysRevD.110.L061307)
- Sfaradi, I., Beniamini, P., Horesh, A., et al. 2024, MNRAS, 527, 7672, doi: [10.1093/mnras/stad3717](https://doi.org/10.1093/mnras/stad3717)
- Short, P., Nicholl, M., Lawrence, A., et al. 2020, MNRAS, 498, 4119, doi: [10.1093/mnras/staa2065](https://doi.org/10.1093/mnras/staa2065)
- Sironi, L., & Giannios, D. 2013, ApJ, 778, 107, doi: [10.1088/0004-637X/778/2/107](https://doi.org/10.1088/0004-637X/778/2/107)
- Takahashi, K., Ioka, K., Ohira, Y., & van Eerten, H. J. 2022, MNRAS, 517, 5541, doi: [10.1093/mnras/stac3022](https://doi.org/10.1093/mnras/stac3022)
- Tchekhovskoy, A., Metzger, B. D., Giannios, D., & Kelley, L. Z. 2014, MNRAS, 437, 2744, doi: [10.1093/mnras/stt2085](https://doi.org/10.1093/mnras/stt2085)
- Teboul, O., & Metzger, B. D. 2023, ApJL, 957, L9, doi: [10.3847/2041-8213/ad0037](https://doi.org/10.3847/2041-8213/ad0037)
- Tingay, S. J., Jauncey, D. L., Preston, R. A., et al. 1995, Nature, 374, 141, doi: [10.1038/374141a0](https://doi.org/10.1038/374141a0)
- van Eerten, H., Zhang, W., & MacFadyen, A. 2010, ApJ, 722, 235, doi: [10.1088/0004-637X/722/1/235](https://doi.org/10.1088/0004-637X/722/1/235)
- van Velzen, S., Gezari, S., Hammerstein, E., et al. 2021, ApJ, 908, 4, doi: [10.3847/1538-4357/abc258](https://doi.org/10.3847/1538-4357/abc258)
- Wu, S. C., Tsuna, D., Mockler, B., & Piro, A. L. 2025, arXiv e-prints, arXiv:2511.14008, doi: [10.48550/arXiv.2511.14008](https://doi.org/10.48550/arXiv.2511.14008)
- Zhang, F., Shu, X., Yang, L., et al. 2024, ApJL, 962, L18, doi: [10.3847/2041-8213/ad1d61](https://doi.org/10.3847/2041-8213/ad1d61)
- Zhuang, J., Shen, R.-F., Mou, G., & Lu, W. 2025, ApJ, 979, 109, doi: [10.3847/1538-4357/ad9b98](https://doi.org/10.3847/1538-4357/ad9b98)
- Zrake, J., Xie, X., & MacFadyen, A. 2018, ApJL, 865, L2, doi: [10.3847/2041-8213/aaddf8](https://doi.org/10.3847/2041-8213/aaddf8)